

Journal of Materials Chemistry A

Accepted Manuscript



This is an *Accepted Manuscript*, which has been through the Royal Society of Chemistry peer review process and has been accepted for publication.

Accepted Manuscripts are published online shortly after acceptance, before technical editing, formatting and proof reading. Using this free service, authors can make their results available to the community, in citable form, before we publish the edited article. We will replace this *Accepted Manuscript* with the edited and formatted *Advance Article* as soon as it is available.

You can find more information about *Accepted Manuscripts* in the [Information for Authors](#).

Please note that technical editing may introduce minor changes to the text and/or graphics, which may alter content. The journal's standard [Terms & Conditions](#) and the [Ethical guidelines](#) still apply. In no event shall the Royal Society of Chemistry be held responsible for any errors or omissions in this *Accepted Manuscript* or any consequences arising from the use of any information it contains.

Visible Light Enhanced Removal of Sulfur Mustard Gas Surrogate from a vapor phase on Novel Hydrous Ferric Oxide/Graphite Oxide Composites

Javier A. Arcibar-Orozco,^a and Teresa J. Bandosz^{a*},

^a Department of Chemistry, The City College of New York, New York, NY 10031 USA

Tel.:(212)650-6017; Fax: (212)650-6107, E-mail: tbandosz@ccny.cuny.edu

Keywords: 2-chloroethyl ethyl sulfide, hydrous ferric oxide, graphite oxide, composites, detoxification.

Abstract

In this work, novel composites of iron hydroxide and graphite oxide (GO), initial or modified with urea, were synthesized and used as media for a 2-chloroethyl ethyl sulfide (CEES) removal/decontamination process. The results of surface characterization, using various physical and chemical methods, indicated that oxygen groups in GO act as nucleation centers for the hydrous ferric oxide formation/aggregation. Addition of the graphene phase increased the surface area and the amount of reactive adsorption centers. The iron hydroxide particles were highly dispersed between and on the graphene layers. Mesoporous 2 and 6-line ferrihydrite with a surface area higher than 200 m²/g, was identified as the main inorganic phase of the composites. An alteration in the optical band gap was found, depending on the chemical properties of the graphite oxide. The composites demonstrated a marked CEES adsorption capacity and outperformed the

unmodified iron hydroxide. Visible light enhanced CEES removal owing to the photocatalytic properties. As a result of this, CEES degradation products migrate to very small pores of the composites, releasing the adsorption centers for further reactive adsorption of the CEES molecules.

Introduction

The Bis(2-chloroethyl)sulfide, also known as mustard gas (HD), is a toxic compound that was used in the past as a chemical warfare agent¹. HD is a vesicant and bifunctional alkylating agent with a high degree of toxicity. It rapidly causes erythema, edema and severe blistering after a short period of exposure². 2-Chloroethyl ethyl sulfide (CEES) is a surrogate of a mustard gas that contains the same functional group (SCH₂CH₂Cl) as HD, which is responsible for alkylation of proteins, and therefore it simulates the toxicological effects of a mustard gas. Exposure to liquid HD or CEES causes a severe skin damage; however, an exposure to its vapors might also cause a temporal or permanent incapacitation¹. Even though one of the mechanisms in which the CEES can be dispersed as a chemical warfare agent (CWA) is by volatilization and generation of vapors, studies on vapor adsorption of CEES are less frequent than those addressing its behavior in aqueous or in organic solutions³⁻⁵. Due to the similarity of CEES to HD and the possibility of using this compound as a chemical warfare agent, there is a large interest in the research on new and efficient detoxification and decontamination technologies.

Hydrolysis of the C-Cl is commonly reported as an important path for the detoxification of the CEES, however, sometimes numerous intermediate compounds are formed on the

surface of catalysts, deactivating them⁵. Alternatively, two of the main products of HD and CEES oxidation are their corresponding sulfones and sulfoxides^{1, 6}. The former ones are less toxic than HD and have a lower vapour pressure. Nevertheless, they still may cause lacrimation and sneezing. On the other hand, sulfoxide is not a vesicant and has less toxicological effects. Since either hydrolysis of the C-Cl bond or oxidation of the S atom reduce the toxicological effect of CEES, these two mechanisms have been investigated as decontamination means in the presence of oxidant materials with photocatalytic activity¹.

The surface of metal oxides is known for its oxidation potential and semiconducting properties⁷. The iron (III) oxides and hydroxides collectively named hydrous ferric oxides (HFO) have been reported to be excellent oxidizing agents for several compounds, including sulfur^{8, 9}. The HFO possess a band gap that ranges from very low (< 0.1 eV) to medium high (2.2 eV) energy value, depending on the crystal structure, crystallinity level and crystal size of the specific HFO¹⁰. It has been demonstrated that hydrous ferric oxides can be photocatalytically active in the visible light range¹¹. Moreover, the HFO have been proven to be excellent adsorbents, due to their porosity and relatively high surface area^{12, 13}. In addition, they can be fast and easily produced on laboratory and industrial scales, using a low cost synthesis process. All of these make them interesting materials for the destruction of toxic compounds.

In recent years a great interest has emerged in the study of graphene-based materials¹⁴⁻¹⁶. Owing to their unique properties they can provide beneficial features to their composites with metal oxides^{17, 18}. Graphite oxide (GO) is formed when a graphite is treated with

strong oxidizing agents, resulting in a material with a large amount of surface oxygen-containing groups attached to the graphene layers¹⁹. Recent literature reports have presented the benefits of graphite oxide addition to metal oxides for various applications of the resulting composites. Seredych and co-workers found an enhancement in the electrical conductivity of zinc hydr(oxide)s after GO addition¹⁶, and an increase in the efficiency of H₂S²⁰ and NO₂²¹ reactive adsorption. This synergistic effect of GO has been also reported as increasing the uptake of H₂S on CuO/GO composites²², the uptake of NO₂ on metal organic frameworks (MOFs)²³, and as enhancing the degradation of methyl orange on TiO₂²⁴.

Morishige and Hamada reported a successful pillaring of α -Fe₂O₃ and Fe₃O₄ between the thin graphene layers. Bashkova and co-workers²⁵ demonstrated the efficacy of this kind of composites for the removal of NO₂ at room temperature, as a result of an increase in the composite surface area after the GO addition. It has also been reported that the electrical conductivity of iron hydroxides changes after the GO addition²⁶.

The chemical composition of GO is an important factor that influences the formation and performance of the composites. Not only did the addition of aminated graphite oxide (GOU) to MOF significantly enhanced the CO₂ adsorption on the composites²⁷ but that adsorption was much higher compared to that on the composite with an unmodified GO²⁷. The superior performance was attributed to the incorporation of amino groups to the edges of graphene oxide that provided reaction sites for copper complexation and thus increased the structural and chemical heterogeneity of the composite products.

Based on the state-of-the-art research results on the GO-containing composites, we hypothesize that owing to the oxidizing and photocatalytic properties of GO and iron oxyhydroxides, the both composites will be capable to efficiently remove/destroy CEES via reactive adsorption. To the best of our knowledge, iron oxyhydroxide composites have not been studied for the detoxification of CEES. Therefore, the objective of this work is to evaluate the decontamination efficiency of a mustard gas surrogate on the graphite oxide/ and aminated graphite oxide/iron oxyhydroxides composites (FeO-GO and FeO-GOU respectively), as well as on the un-modified iron oxyhydroxide (FeO). An extensive surface characterization of iron/oxyhydroxides/graphite oxide and iron/oxyhydroxides/aminated graphite oxide composites was conducted, and the physicochemical properties of the materials were linked to their capacity for the reactive adsorption of CEES.

Results and discussion

To evaluate if the treatment with urea changed the surface chemistry of GO, the following analyses were carried out on initial and modified samples: X-Ray powder diffraction (XRD), Fourier transform infrared spectroscopy (FTIR), and potentiometric titration. The results are summarized in Figure 1. The XRD patterns show an increase in the intensity of the peak at $43^\circ 2\theta$ associated with graphite (121^{28}), which suggests the possibility of graphite oxide reduction after urea treatment. The d_{002} in the GO changes from 9.6 to 7.9 after urea exposure, indicating a decrease in the interlayer distance due to the reactions of urea with GO functional groups²⁹ (Figure 1A). The FTIR spectra reveal the characteristic

bands of the GO oxygen functional groups³⁰ at 1726, 1621, 1047 and 985 cm^{-1} (Figure 1B). The band at 1228 cm^{-1} can be attributed to S=O asymmetric stretching vibrations of sulfonic groups³¹, due to the application of sulfuric acid for graphite oxide oxidation¹⁴. After urea treatment there is a shift in the wavenumbers of the bands corresponding to the carbonyl groups, meanwhile the band at 1621 cm^{-1} is detected at 1616 cm^{-1} . These changes indicate a change in the chemical environment of the oxygen groups that are interacting with amine groups in the urea. The band at 1616 cm^{-1} might also be due to N-H bending vibrations characteristic of secondary amines³².

Another evidence of the graphite oxide amination is provided by the titration experiments. The proton binding curves (Figure 1C) show an increase in the alkalinity of the surface of GOU and a slight but repeatable and consistent change in the surface pH (from 2.08 to 2.24). The increase in the basic properties of the graphite oxide is also demonstrated in the shift in the pK_a positions (Figure 1D) of some oxygen functionalities (marked with arrows), especially the ones at high acidity. We link it to their reactions with amine groups²⁹. In both samples, groups having pK_a between 10 and 11 predominate. We assign them to the OH/phenolic groups of GO and GOU³³. In the later sample some basic nitrogen surface compounds can also contribute to these species.

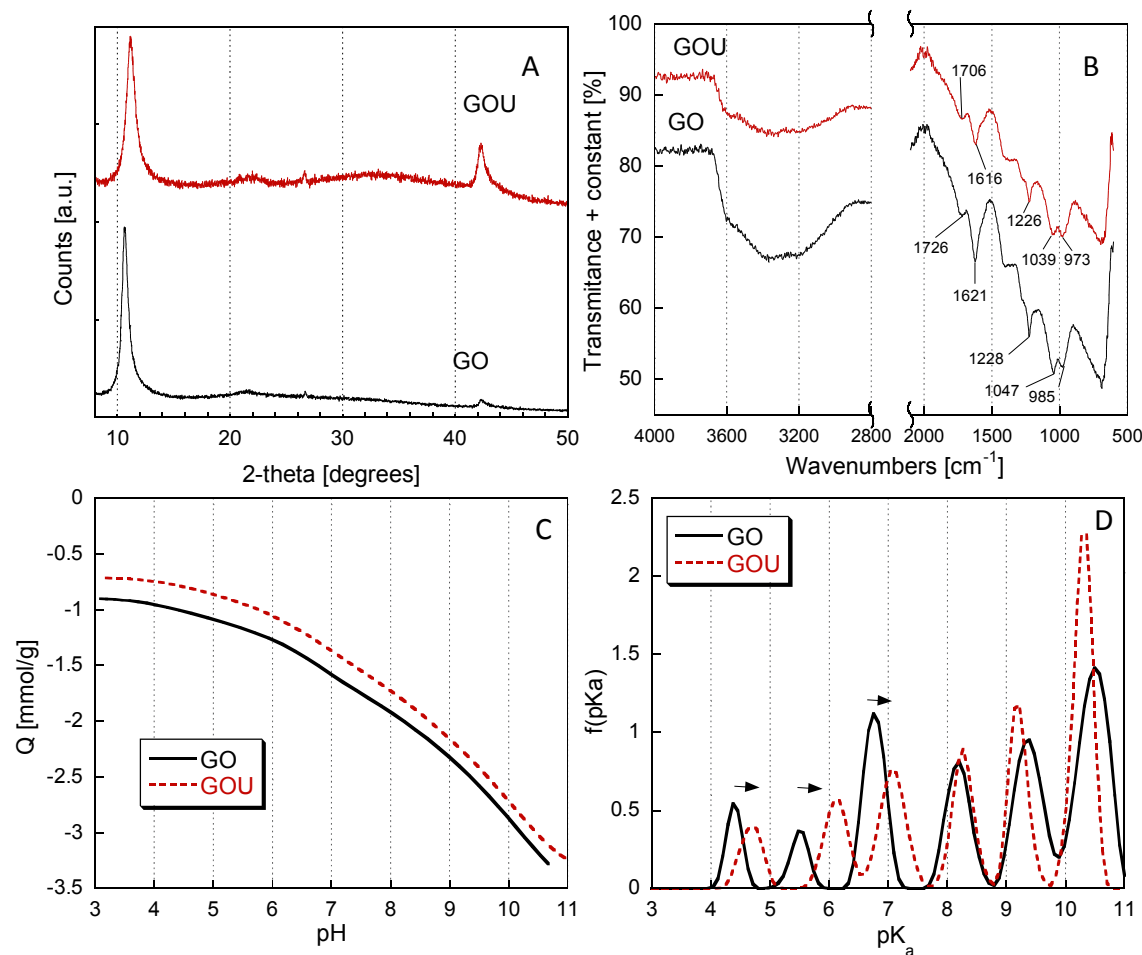


Figure 1. A) X-Ray diffraction patterns, B) FTIR spectra, C) Proton binding curves and D) pKa distributions for the graphite oxide (GO) and aminated graphite oxide (GOU).

The parameters of the porous structure of the materials studied are collected in Table 1. The surface area (S_{BET}) of FeO is considered as being high and it is in the range of those for other HFOs reported in the literature (e.g. $230 \text{ m}^2/\text{g}^{34}$). Those high surface areas are typical of highly amorphous materials, mainly 2-line ferrihydrite. The total pore volume (V_{T}) is greater than $0.25 \text{ cm}^3/\text{g}$, and mainly mesopores contribute to this value. The addition of GO and GOU increases the porosity. In the former case the surface area increases to $243 \text{ m}^2/\text{g}$ (21%), which is linked to increases in the total volume of pores (15%) and in the volume micropores (V_{mic}) (19%). For the composite with GOU, there is

even a greater increase in the surface area ($88 \text{ m}^2/\text{g}$; 44 %). The micropore and total pore volumes increase 17% and 40%, respectively. Even though the ratios of the mesopore to micropore volumes in all composites remain higher than 2, the smallest value for FeO-GOU suggests its least mesoporous character.

Table 1. The parameters of porous structure calculated from nitrogen adsorption isotherms.

Sample	S^{BET} [m^2g^{-1}]	V_{T} [cm^3g^{-1}]	V_{mic} [cm^3g^{-1}]	V_{meso} [cm^3g^{-1}]	$V_{\text{meso}}/V_{\text{mic}}$
FeO	200	0.265	0.073	0.192	2.6
FeO-GO	243	0.304	0.087	0.217	2.5
FeO-GOU	288	0.312	0.102	0.210	2.1

Pore size distributions calculated from the nitrogen adsorption isotherms are compared in Figure 2A. The distribution for FeO shows that the predominant pore size is 4 - 5 nm, demonstrating the mesoporous nature of the pure hydrous ferric oxide. The PSDs for the composites are similar to that for FeO in the shape, although the pore volume increased. Another important feature is a shift in the predominant pore size to smaller values for the composite with GOU, and the appearance of pores with sizes of about 2.5 nm. Kaiser and co-workers³⁵ reported that the uptake of CEES from a solution of hydrofluoroethers on commercial activated carbon fabrics was the most efficient on those with a mean pore size of 2.9 nm. Depending on the mechanism of decontamination, the mesopores of these

sizes could also play an important role in the reactive adsorption of CEES on our materials.

The high surface area of the composites is also affected by their specific crystallographic structure. X-Ray diffraction patterns are collected in Figure 2B. The XRD pattern of FeO shows broad peaks at 35, 40, 53, 59 and 63 2θ that correspond to a small crystal size 6-line ferrihydrite (110, 112, 114, 115 and 300 Miller indexes respectively³⁶), or a metaphase between 6-line and 2-line ferrihydrite³⁷. The size of the crystallites calculated using Scherrer is about 2.9 nm (See details in Supporting Information), which is an indication of the microcrystalline nature of this material³⁸. Besides the peaks associated with ferrihydrite, the diffraction pattern of FeO also reveals low intensity peaks corresponding to akaganeite at 21 (110), 27 (311), 40 (211) and 46 (301). The existence of this crystallographic phase might be linked to a minor transformation of 2-line ferrihydrite caused by the precursor salt and partial dehydration taking place during the synthesis process (temperature effect)³⁷.

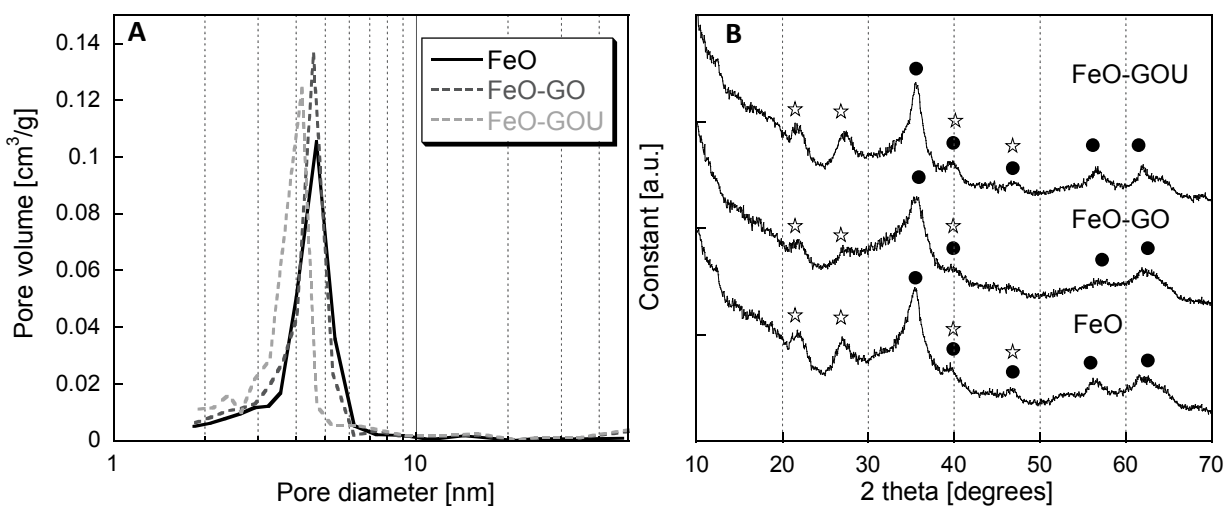


Figure 2. A) Pore size distributions for the ferric hydrous oxide and the composites with graphite oxide. B) X-Ray diffraction patterns of the hydrous ferric oxide and the composites with graphite oxide, ● 6-line ferrihydrite, ☆ -Akaganeite.

After the GO addition there is a marked change in the crystallographic pattern, and only the broad peaks at 35 and 63 2θ are visible indicating the presence of 2-line ferrihydrite. The peaks corresponding to akaganeite decreased in their intensity, suggesting that GO inhibits the minor transformation of the 2-line ferrihydrite. Applying the Scherrer equation gives a crystallite size of about 2.1 nm. This implies that GO induces a decrease in the particle size of the inorganic iron hydroxide phase. After GOU addition the XRD pattern is similar to that for FeO with the main crystallite size of 4.0 nm. Thus the addition of GOU does not considerably change the crystal structure of the composite. It only alters its porosity.

The Scanning Electron Images (SEM) images of the composites are collected in Figure 3. The FeO shows a rugous surface with large pores formed between small clusters of rounded shape nanoparticles ranging between 60 and 110 nm (as shown in the rectangle). The shape of the particles is characteristic of 6-line ferrihydrite³⁹. The images suggest that the presence of GO in the FeO-GO composite increased the apparent level of amorphicity, since the round-shaped nanocrystals detected are in the range of 20-70 nm, 50% smaller than those in FeO.

The morphology of FeO-GOU differs from those of FeO and FeO-GO. In this material the presence of the graphene layers of the aminated graphite oxide is evident. Small particles are visible in the vicinity of the layers. A filtered image of the selected area in the FeO-GOU shows the presence of the graphene layers in the composite and the hydrous iron oxide particles deposited on their surface.

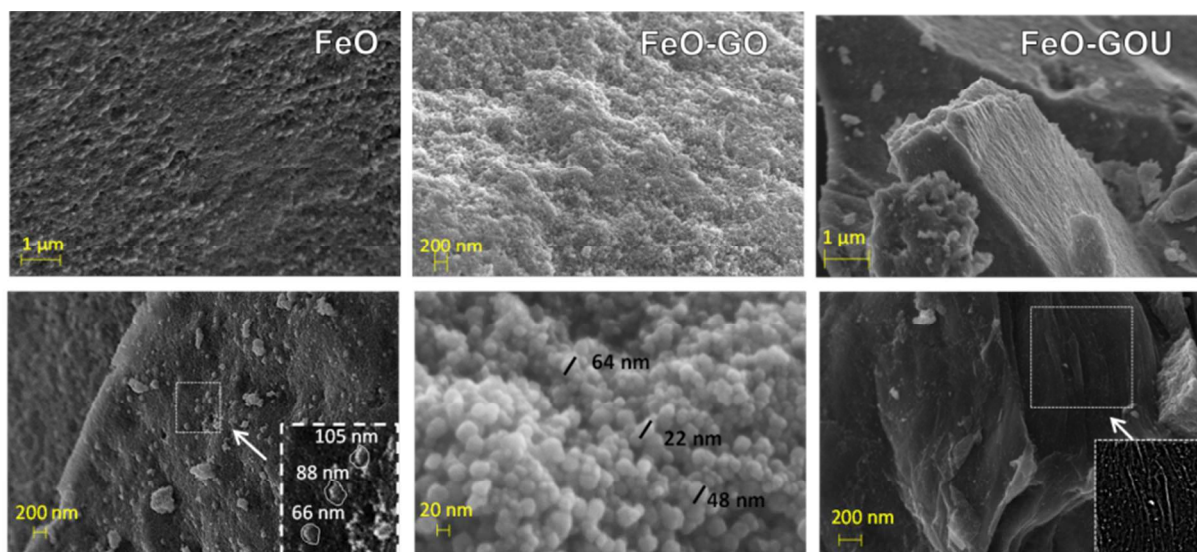


Figure 3. SEM images of the surfaces of the samples studied. The enlarged area in the image of FeO-GOU corresponds to a band-pass filter image obtained applying Fast Fourier Transform (FFT) of the area marked in the square. A mask removing at high and low frequencies was applied, and the inverse FFT yielded the band-passed image (See Supplementary Information for detail of the image processing).

The differences in the morphology of the composites are also evident from HRTEM images presented in Figure 4. FeO exhibits a marked, amorphous nature, showing the typical structure of 2-line ferrihydrite (Figure 4A). The image also reveals the presence of ordered structure around the amorphous phase (Figure 4B), which we link to the graphene

based phase embedded within the amorphous structure of the 2-line ferrihydrite. In the case of FeO-GOU clusters of particles of about 100-200 nm with some crystallinity level are seen, as observed in the electron diffraction pattern (Figure 4C and 4D). As mentioned above, in this sample the 6-L ferrihydrite is present and therefore the crystallinity can be attributed to this phase. The crystal sizes of about 3-5 nm (Figure 4E) are in agreement with the XRD results. Lattice spacing is of about 0.23 nm, (Figure 4F, insert) and it corresponds to the (110) d-space of 6-line ferrihydrite¹⁰.

The particle size found based on the TEM images of FeO-GOU is slightly larger than that calculated from the Scherrer equation. This is due to other factors (besides particle size) that influence the peak broadening, such as dislocations and lattice imperfections. However, both methods give the sizes of similar magnitudes and both of them confirm the nanoscale range of our materials.

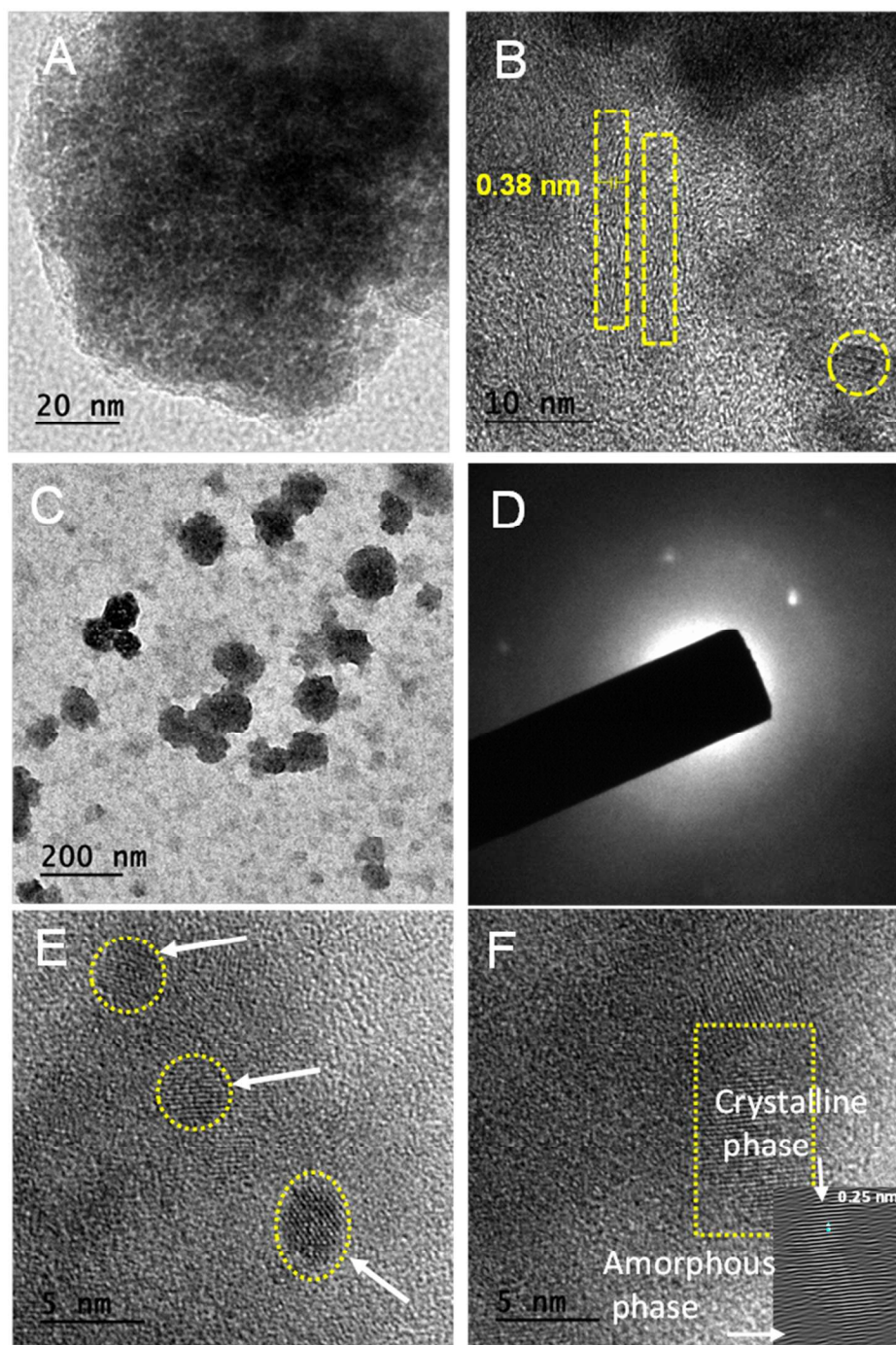


Figure 4. A) TEM image of FeO-G, B) a highlighted zone showing the graphene phase in the FeO-GO and a small crystal of the iron hydroxide phase. C) TEM image of FeO-GOU. D) Electron diffraction pattern revealing some degree of crystallinity in the samples. E) Image of the FeO-GOU nanocrystals. F) Image of the nanocrystals, the inset

represents the inverse Fourier transform of the selected area, the fridge distance is of 0.25 nm.

Not only the morphology, but also the surface chemistry of the iron oxyhydroxides are affected by the addition of GO and GOU. The proton binding curves (Q) and the pK_a distributions for the samples studied show the marked differences in surface chemistry (Figure 5). The proton binding curve for FeO shows a negatively charged surface with a point of zero charge (pH_{PZC}) of 7.5, that is in the range of hydrous ferric oxides, especially ferrihydrites^{10, 40}. The addition of GO or GOU acidifies the surface of the composites and causes a shift in the pH_{PZC} to 6.8. This can be caused by the contribution of acidic groups from the graphite oxide or changes in the chemical environment of iron containing acidic groups on the interface between the GO and hydroxide phases. These changes are less pronounced for the composite with GOU than for that with GO.

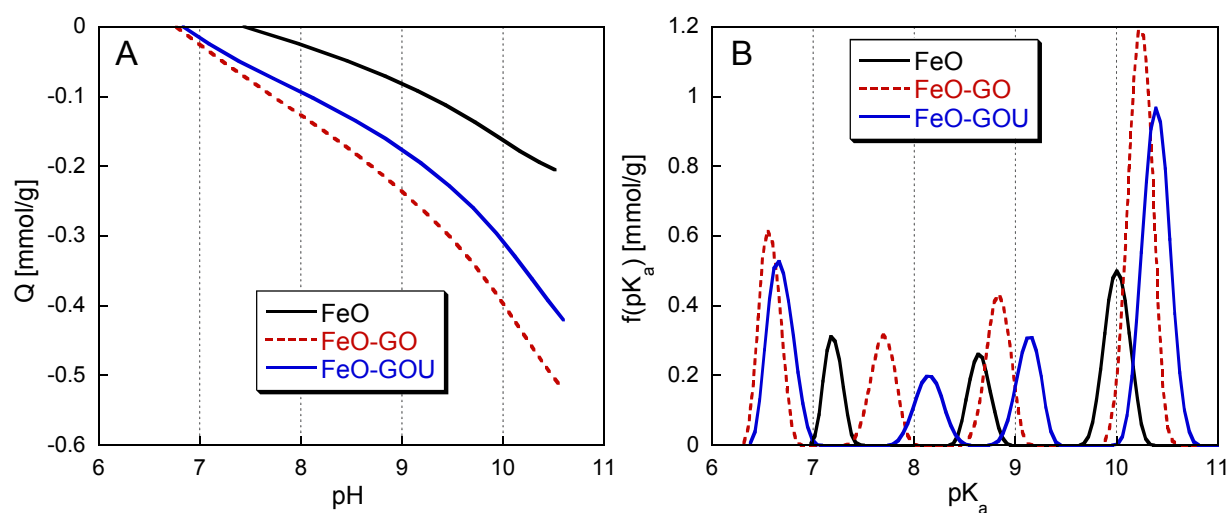


Figure 5. Potentiometric titration results: proton binding curves (A) and pK_a distributions (B).

The pK_a distribution in Figure 5B provides more details on the surface chemical changes caused by the GO and GOU additions. For FeO three species at pK_{as} 7.1, 8.6 and 10 are revealed. The ones at 7.1 and 8.6 might correspond to the acidity constants of the protolysis reactions of the OH surface groups of the ferrihydrite¹⁰; and the one at 10 can be attributed to the presence of polynuclear Fe(III) (hydroxyl) species⁴¹. On the surface of FeO-GO new groups at pK_a of 6.6 appear, and the species represented by pK_a between 7 and 8 and between 8 and 9 in the case FeO have developed a more basic character. Also, the contribution of the most basic group at $pK_a > 10$ representing terminal hydroxyl groups clearly increases. This increase is likely caused by an increase in the amorphicity level of the inorganic phase and thus more terminal hydroxyl groups on the surface³⁷. The OH groups of GO can also contribute to these values. In the case of the FeO-GOU, the peak at pK_a 6.6 is still present; however there is a greater shift in the position of the peaks attributed to the presence of the OH groups from ferrihydrite to 8.1 and to 9.1. The population of species at pK_a 10.5 increases compared to those on FeO but their contribution seems to be smaller than that for FeO-GO. The total number of groups in the composites with GO and GOU increased 250 % and 220 %, respectively, when compared to the numbers of acidic groups detected on FeO (Table S1 in Supplementary Information).

The FTIR-ATR spectra (Figure 6) show subtle but interesting differences between the composites. Two bands are observed for all samples; the one at a wavenumber of 3410 cm^{-1} corresponds mainly to stretching of OH bulk groups in the ferrihydrite structure⁴², and the band at 1650 cm^{-1} corresponds to adsorbed water⁴³. Low intensity bands at 1469

and 1353 cm^{-1} can be attributed to Fe-O and Fe-OH, respectively⁴². Finally the band at 694 cm^{-1} corresponds to the deformation of bulk hydroxyl groups coming from the hydrated ferric oxides³⁷. For FeO-GO a band at 1598 cm^{-1} appears that might be linked to remaining carbonyl groups of GO. A band at 1336 cm^{-1} represents the shift of the Fe-OH band due to a change in the chemical environment caused by the GO addition. The same assignment applies to the band at 684 cm^{-1} that corresponds to iron hydroxyl groups' deformation.

In the composite synthesized with GOU there is a decrease in the intensities of the bands representing Fe-O bonds, and the band corresponding to GO carbonyl groups disappears. As for the composite with GO, the Fe-OH band shifts to 1332 cm^{-1} and that associated with the hydroxyl groups is shifted to 670 cm^{-1} . Also there is the appearance of a small shoulder at a wavenumber of 910 cm^{-1} . This band might correspond to the N-H wagging of primary and secondary amines in GOU⁴⁴.

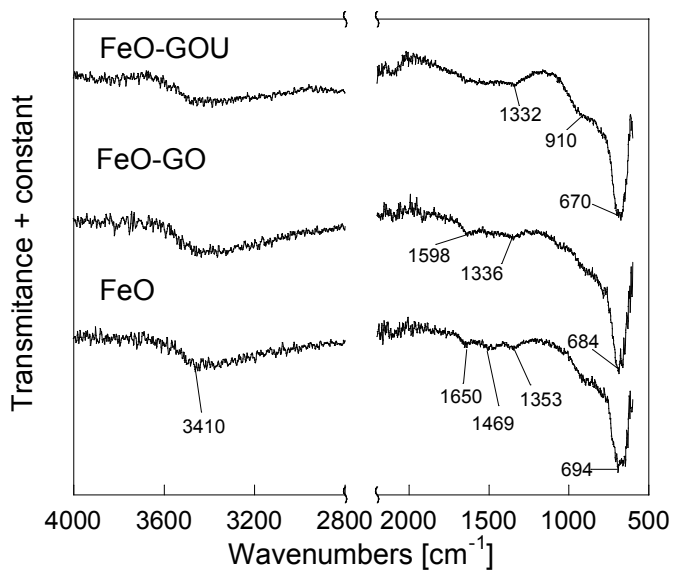


Figure 6. FTIR-ATR spectra for the materials studied.

The FTIR results suggest the interaction of iron with oxygen groups of GO. This is in agreement with other studies that have reported reactions of GO oxygen groups (mainly epoxy) with metal oxide surfaces²²⁻²⁴.

The changes in the chemistry of our materials were also studied by Raman spectroscopy (Figure 7). The Raman spectrum of FeO reveals weak bands at 500 cm^{-1} and 1230 cm^{-1} , and a strong band at 715 cm^{-1} , that correspond to those reported for 2-line ferrihydrite⁴⁵. In the spectra for the composites with GO and GOU, the bands assigned to the carbon phase appear; one at 1320 cm^{-1} that is related to the disorder in the graphene layers (D band), and one at 1590 cm^{-1} that is attributed to the sp^2 domains in graphene lattice (G band)⁴⁶. It is important to mention that for the composite formed with GOU, the D and G bands are less intense and wider than those for FeO-GO. A I_D/I_G ratio for the composite with GO is 0.97 and for that with GOU - 0.83. It is well known that a higher disorder in graphite leads to broader G bands and a larger I_D/I_G ratio⁴⁷. Thus a higher I_D/I_G ratio and a broadened G band for the composite with GO than for that with GOU indicates its higher level of structural defects. These results are in agreement with the SEM images in which the GOU surface shows a layered structure that has fewer visible defects than the GO. The presence of structural defects in the graphene phase of the composites affects their electronic properties⁴⁸. Even though the GO addition is expected to enhance the electron transport in the composite, a presence of structural defects might change the electron trajectories⁴⁹. On the other hand, the amination of graphite oxide led to a layered composite with less structural defects, and therefore a better electron transport. These

features might be important for potential redox reactions taking place on the surface of these materials. Owing to these differences in the morphology, it is expected that the composites with GO and GOU will perform in a different way as the CEES adsorption/degradation media.

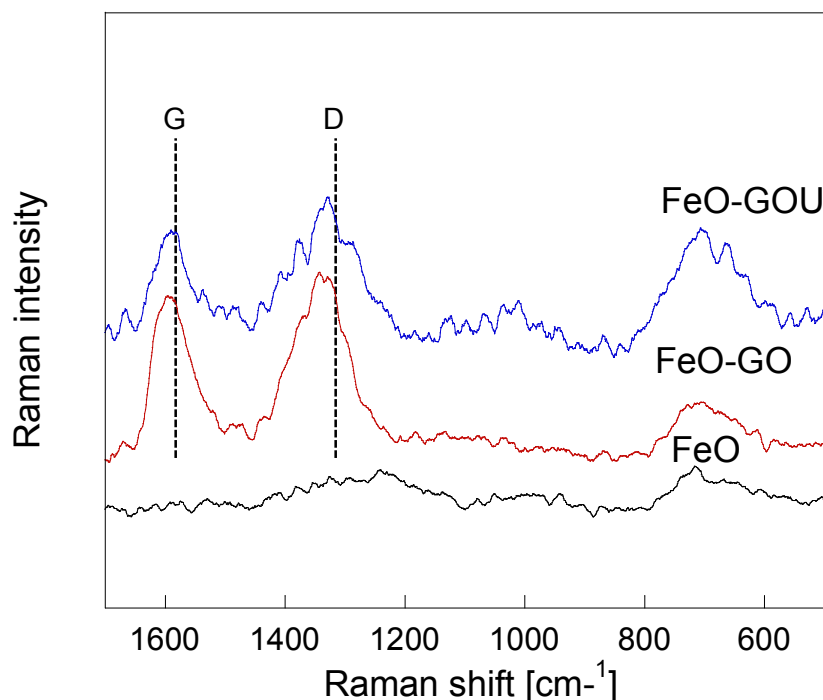


Figure 7. Raman spectra of FeO and its composites with GO or GOU.

The Ultraviolet-Visible-Near Infrared Spectroscopy (UV-Vis-NIR) spectra of the composites are shown in Figure 8A. The shoulder at 760 nm originates from the electronic transitions of Fe³⁺ ligand field, and magnetically coupled Fe³⁺ cations and also from ligand-to-metal charge transfer (LMCT)⁵⁰. The difference in the maximum and minimum absorption branches after the GO and GOU additions is a result of the change in the chemical environment caused by the incorporation of graphene layers to the composite²⁹. Since any change in the material's physics and chemistry has an effect on

the band gap width, the band gap energy (E_g) was estimated from the UV-Vis-NIR spectrum⁵¹. Details of the E_g calculation are provided in the Supplementary Information. The extrapolation of the linear fit of the plot of $[F(R_{\infty})hv]^2$ versus the photon energy ($h\nu$) yields the value of the E_g . The plots are shown in Figure 8B.

The calculated band gap energy of the FeO is 1.74 eV; which is in the range of poorly crystallized hydrous iron oxides³⁷. On the other hand, the samples with GO and GOU exhibit energy gaps of 1.63 and 1.79 eV, respectively. Therefore, the addition of GO decreases the extent of E_g , and in the case of the aminated graphite oxide, a slight increase is caused by the addition of GOU. These different effects on the optoelectronic properties of the composites, depending on the chemical nature of the graphite oxide, are associated with the specific interactions of the hydrous ferric oxides and the graphite oxide.

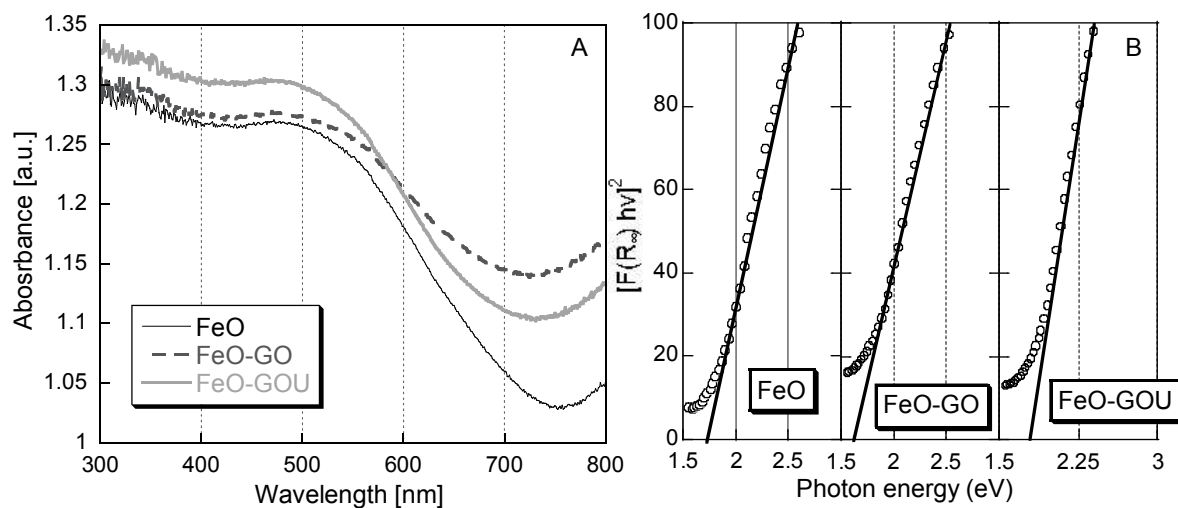


Figure 8. **A)** UV-Vis-NIR spectra of the synthesized composites, **B)** $[F(R_{\infty})hv]^2$ versus photon energy. The lines show the cut-off employed to calculate the band gap energy.

Since FeO-GO, absorbs a broader range of visible light, graphite oxide is photosensitizing the composite. This effect has been observed for wide band semiconductors in which the band gap is not able to be photoexcited, and no holes are formed; in those cases the graphene phase acts like a macromolecular photosensitizer⁵². For Fe-GO it is possible that GO is photoexcited to such a state that it injects electrons into the conduction band of the hydrous ferric oxide. This process promotes the activation of oxygen and the formation of oxide radicals⁵². On the other hand, the FeO-GOU material shows an absorption at lower wavelengths close to the NIR range, and also a higher absorption at wavelengths lower than 550 nm. It has been reported that this effect occurs due to the abundance of delocalized electrons in the graphite network, which might enhance charge transport, and promote the formation of holes and electrons in the composite materials^{20, 53}. It is possible that in this composite the carbon phase may act as a trap for the formation of holes in the irradiated composites⁵⁴. It has also been reported that nitrogen doping into Cu₂O films increases E_g , due to the structural changes that generate numerous oxygen vacancies⁵⁵. Also, the incorporation of nitrogen moieties into the graphene matrix shifts the Fermi level and contributes to breaks in the symmetry of the graphite lattices, therefore causing an opening of the E_g ⁵⁶. It is possible that the combination of these effects takes place in the FeO-GOU composite. Both effects, photosensibilizing and narrowing of the band gap, can be beneficial for the process of the CEES/oxidation/degradation. While wide band gap semiconductors have a good carrier mobility⁵⁷, narrow band gap materials are more active in the visible spectrum. It is important to mention that the small differences between the energies might be statistically insignificant. Nevertheless, the values of the band gap energies for our samples suggest their photoactivity in visible light.

Based on the results obtained, it is suggested that in the FeO-GO composite, HFOs were incorporated into the composite via interaction with oxygen groups located in the graphite oxide network structure. The incorporation mechanism can be explained as follows: at the first stage, the interactions of the iron hexaaquo complexes in solution with the oxygen groups in the GO to form oxygen bridges take place (Figure 9A); when the pH increases, in the second stage, the oxygen groups in the graphite oxide act as nucleation centers for the propagation reactions of the iron complexes to form HFOs (Figure 9B). The propagation stage occurs when the increase in the pH causes the condensates to aggregate⁵⁸ (Figure 9C), thus promoting the formation of particles around the graphite oxide layers (Figure 9D). In the current experimental conditions (concentration of the precipitation agent and addition rate), the particles are formed as an apparently amorphous phase consisting of microcrystals with a high surface area and mesoporosity. A 24 hours equilibrium time was established as an acceptable time to reach total CEES evaporation which led to a constant concentration in our systems (See Figure S2 in Supplementary Information). After a 24 h duration of the adsorption process, an increase in the weight of the composites was recorded (Q^{ads}). It represents the capacity of the system to adsorb CEES and/or its reaction products. Besides the experiments in visible light, the experiments in the dark were also carried out to determine if the redox reactions stimulated by visible light might affect the adsorption capacity of the composites, or promote reactions that might result in a change in the adsorption capacity of our materials.

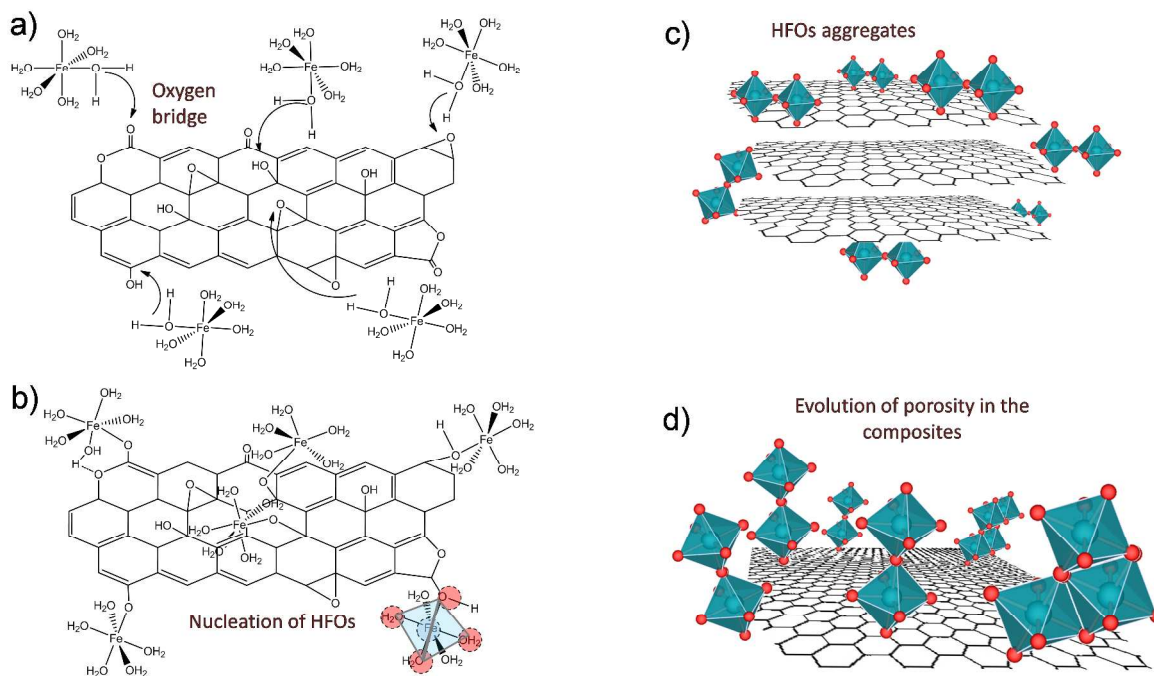


Figure 9. Interactions of HFO with GO surface, A) Nucleation of iron hexaquo complexes, B) oxygen bridge between oxygen groups in the GO and iron complexes, C) Condensation of the hydrous ferric oxide particles, and D) Evolution of porosity in the HFO aggregates.

Table 2 collects the increases in the weight of the materials after CEES exposure. As mentioned above, these amounts include both the adsorption of CEES, and of all non-volatile compounds produced during reactive adsorption that might be deposited in the pore system. The uptakes on the composites are visibly higher than those on the pure hydrous oxides, either in the light or dark experiments. Exposure to visible light for 24 hours increases the amount adsorbed by 43 % and 100 % on the composite with GO and GOU, respectively, in comparison with the amount adsorbed on FeO. Interestingly, that increase in the dark experiments after 24 hours was of 40 % and 48 %, respectively. This indicates the strong effect of light, especially in the case of FeO-GOU.

The increase in the exposure from 24 h to 7 days further increases the amount of CEES/ its decomposition products adsorbed (Table 2). It is possible that this can be due to surface mediated slow transformations of molecules from the vapor phase followed by their reactive adsorption. The largest increase was recorded for the FeO-GOU, whose high surface area and pore volume promotes the deposition of the reaction products on the surface. The graphene phase has a positive effect on the enhancement of the CEES reactive adsorption under visible light exposure. Thus for FeO an increase in the weight after 24 hours was 18%, and for the composites with GO and GOU 20 % and 61%, respectively, in comparison with the corresponding results obtained after adsorption in the dark.

To understand the role of the surface features of our materials in the reactive adsorption process, the relationship between the adsorption capacities and the micro- (V_{mic}) and total pore volume (V_T) of the composites was analyzed (Figure 10). The adsorption capacities measured in visible light show almost a linear dependence on the micropore volumes ($R^2 = 0.99$). Apparently the total pore volume is less important for this process ($R^2 = 0.81$). On the other hand, the results obtained in the dark experiments show a perfect correlation with the total pore volume ($R^2=0.99$) and much less dependence on the volume of micropores ($R^2 = 0.86$).

Table 2. An increase in the weight of the composites/amount adsorbed after CEES exposure under visible light and in the dark together with the adsorption capacities and the percentages of

CEES removed and transformed into volatile compounds on the surface of the samples studied after 7 days of experiments under visible light exposure.

Samples	Q^{ads} (mg of gained weight g-adsorbent ⁻¹)			Q^{rem} (g g ⁻¹)	M^{rem} (%)	M^{ad} (%)	Volatile (%)
	Light - 24h	Light - 7 days	Dark- 24h				
FeO	86	193	73	0.67 ^{a)}	32 ^{a)}	9 ^{a)}	23 ^{a)}
FeO-GO	123	174	102	1.26 ^{a)}	58 ^{a)}	7 ^{a)}	51 ^{a)}
FeO-GOU	174	228	108	1.31 ^{a)}	61 ^{a)}	9 ^{a)}	52 ^{a)}

^{a)}Obtained after 7 days of contact.

Initially adsorbed CEES, besides being retained on the surface via dispersive forces, can also be transformed either into small gaseous molecules non-adsorbed on the materials' surfaces, or can undergo surface reactions with their products adsorbed in the pore system. Regardless of its fate, the analysis of the concentration of CEES in headspace of the reactors (C_{eq}) should indicate the total disappearance of this adsorbate. To better evaluate its fate, the quantities listed below were introduced:

The capacity of CEES removal (Q^{rem}) was calculated according the formula:

$$Q^{rem} = \frac{C_0 - C_{eq}}{m} * V_C \quad (1)$$

Where C_0 stands for the initial concentration of CEES that was injected to the system and m for the mass of the adsorbent before CEES exposure.

The total CEES removal capacity (M^{rem}) can be calculated as a ratio between starting and final CEES concentration.

$$M^{rem} = \frac{C_0 - C_{eq}}{C_0} * 100\% \quad (2)$$

Finally, the percentage of adsorbed molecules (M^{ad}) is calculated as follows:

$$M^{ad} = \frac{Q^{ad} * m_0}{C_0 * V_c} * 100\% \quad (3)$$

The percentage of volatile non-adsorbed molecules (*Volatile*) can be calculated as the difference between the percentage of CEES removed (M^{rem}) (which was either adsorbed or decomposed), and the percentage of the adsorbed molecules (M^{ad}). The percentage of the molecules transformed into volatile compounds was calculated according the formula:

$$Volatile = M^{rem} - M^{ad} \quad (4)$$

Even though it is judged based on the unchanged concentration of CEES that its adsorption reaches an apparent equilibrium after 24 h, it is possible that slow surface reactions between compounds formed from the CEES are still taking place on the surface of the adsorbents as hypothesized above. Following this assumption, we ran the experiments for seven days to promote more complete transformations of the molecules. After 24 hours, the concentration of CEES in the headspace and the increase in the weight were evaluated. Results are collected in Table 2.

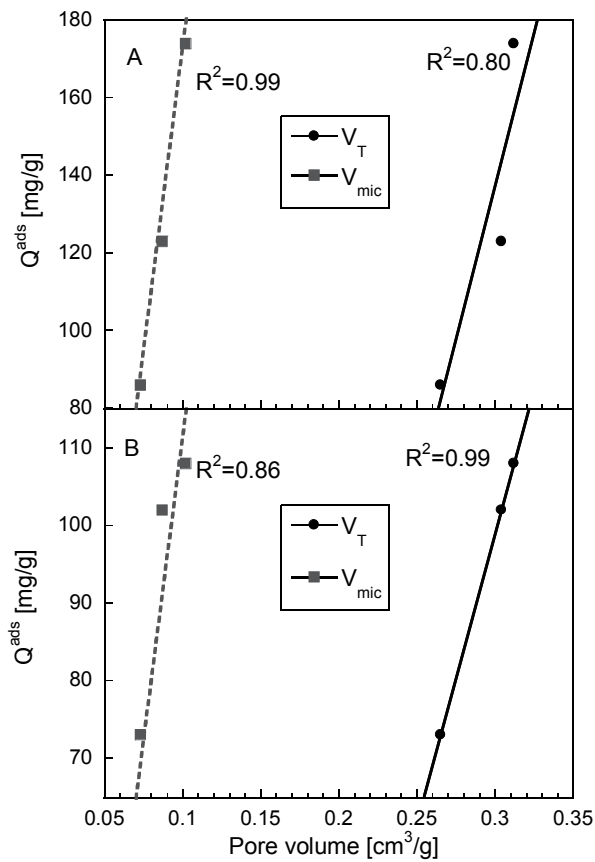


Figure 10. Dependence of the amount adsorbed (after 24 h of equilibrium) on the volume of pores in the materials after CEES exposure. A) under the light exposure; B) experiments in dark.

The materials studied show a high capacity for the elimination of CEES. While on FeO 32% CEES from the reactor volume was adsorbed, the addition of GO increased this amount to 52%. The beneficial effect is reflected also in an increase in the percentage of CEES converted to volatile, non-adsorbed surface reaction products.

The formation of new compounds, as a result of photoactivity, might explain the trends found on the dependence of the Q^{ad} and the volume of specific pores discussed above

(Figure 2A). If light promotes the hydrolysis of C-Cl bonds and therefore the transformation of CEES into smaller molecules, then it is plausible to assume that those small molecules would migrate to narrow pores (micropores) that are less accessible to the larger molecules, such as the CEES. In the gaseous phase the CEES molecule has a critical diameter of 0.58 nm³⁵, small enough to migrate to the materials' micropores. However, in the presence of atmospheric water, the solvation of the molecule results in a molecular diameter of 1.88 nm³⁵. Therefore it is expected that mesopores play a relevant role as reactive adsorption centers for CEES, while micropores are more important for smaller molecules which could be the products of surface reactions/CEES decomposition.

In the absence of light, the extent of CEES transformation is smaller, due to the lack of energy that might promote redox reactions; therefore mesopore sizes are favorable for the accommodation of adsorbed molecules on the surface³⁵. Thus a better correlation of the amount adsorbed with the total pore volume was found.

The results suggest that several reactions between the CEES and the surface of the materials are taking place simultaneously. However, the specific identification of the products of the CEES reactive adsorption, as well as the detailed mechanism of decontamination, is beyond the scope of this paper and it is the focus of our ongoing study. Regardless of the removal mechanism, it is noteworthy to mention that our composites exhibit the marked CEES removal capacity, which makes them promising materials for the decontamination of CWA.

Experimental

Materials: Commercial graphite (from Aldrich) was oxidized using Hummers method⁵⁹. Briefly, commercial graphite (20 g) was mixed with concentrated sulfuric acid (230 mL) at 0 °C, next potassium permanganate (30 g) was slowly added by keeping the reaction temperature below 20 °C in a cooling bath. After, deionized water (230 mL) was slowly added to prevent the temperature from exceeding 98 °C. The colloid was stirred for 15 min, followed by a dilution to 1.4 L, and finally H₂O₂ (100 mL, 30%) was added. The mixture was left to settle overnight and then rinsed until no remaining SO₄⁻² ions were detected. The brown precipitate was freeze-dried during 2 weeks and then stored at -4 °C before use. This material is referred to as GO. The aminated graphite was obtained by mixing GO (1 g) with a urea solution (100 mL, 0.3 M). The mixture was maintained under continuous stirring for 24 h, and then rinsed with deionized water until a constant pH. Finally, the resulting material was air dried at room temperature; the sample is referred to as GOU. The hydrous ferric oxide (FeO) particles were obtained by a precipitation method. FeCl₃·6H₂O (350 mL, 0.026 M) and NaOH (660 mL, 0.05M) were used. The NaOH was added using a Titronic Universal (SCHOTT) titrator at a rate of 40 mL min⁻¹. After the red-brown precipitate was formed, it was rapidly decanted, then rinsed several times with deionized water until no AgCl precipitate was present in the rinsing solution after AgNO₃ addition. Finally, the FeO sample was dried during 24 h at 100 °C. To prepare the composites, GO or GOU was added to the composites to reach a mass content of 10% of the final materials. Either GO or GOU were mixed with FeCl₃·6H₂O (350 mL, 0.026 M) solution. The suspensions were sonicated for 1 h to promote graphite oxide dispersion, and then stirred for an extra hour to increase

homogeneity. After that, NaOH (660 mL, 0.05M) were added at a rate of 40 mL/min. The precipitate was collected and rinsed until no chloride presence was detected, and finally dried at 100 °C for 24 h. Samples are referred to as FeO-GO and FeO-GOU, depending on the type of GO used.

Determination of porosity: The surface area and porosity of the materials studied were calculated from N₂ adsorption isotherms measured using ASAP 2020 (Micromeritics). The BET surface areas were calculated from the isotherms. The total pore volume was obtained from the amount adsorbed at a relative pressure of 0.99 and the micropore volume was calculated from the Dubinin-Astakhov equation⁶⁰. The mesopore volume was calculated by the difference between the V_T and V_{mic} and the Barret-Joyner-Halenda (BJH) was used to calculate pore size distributions, PSDs⁶¹.

X-ray diffraction: The X-Ray powder diffraction patterns were collected from 10 to 90 ° 2θ at absolute scan on a Philips X'Pert X-Ray diffractometer with CuKα radiation at 40 mA and 40 kV.

SEM: The SEM of the surface of the materials, were obtained in a Zeiss Supra 55 VP instrument, with an acceleration voltage of 5 keV.

TEM: The TEM images were obtained in a JEOL JEM-2100 Transmission Electron Microscope operated at 200 kV. Before analysis, the sample was ground, suspended in high purity isopropanol and sonicated for 20 min. After, sample drops were applied to a grid holder.

Potentiometric titration: Potentiometric titration measurements were carried out in a DMS Titrimo 716 automatic titrator (Metrohm). The experimental procedure was as follows: the sample (100 mg) was mixed with a NaNO₃ electrolytic solution (50mL, 0.01M) and

equilibrated during 12 h. The solution was purged with N₂ and when a constant pH was reached, a titration with NaOH (0.1 M) was carried out. During the titration the solution was continuously purged with N₂ to eliminate interference of atmospheric CO₂. The experimental titration curves were transformed into proton binding curves (Q) using a proton balance with a theoretical blank reference⁶². The Q represents the total amount of protonated sites on the surface of the materials. The intercept of the x-axis represents the point of zero charge of the materials (pH_{PZC}). Q values that are below the zero line indicate proton release related to surface acidity. The Q is related to the pK_a distribution of all dissociated groups in the solid by the following equation⁶³:

$$Q(pH) = \int_{-\infty}^{\infty} q(pH, pK_a) f(pK_a) dpK_a \quad (5)$$

Application of this equation yields the pK_a distribution for the species present on the surface, The integral equation was solved using SAEIUS software⁶⁴.

Surface pH: The surface pH was measured by mixing 0.1 g of the material with 5 mL of distilled water and stirring overnight. After, the pH of the solution was recorded.

FTIR: The analyses were carried out in a Nicolet Magna-IR 380 spectrometer, by using the Smart MIRacle accessory that measures the attenuated total reflectance The spectrum was collected 64 times and corrected for background noise. Experiments were done without KBr addition.

Raman spectroscopy: Raman spectra studies were carried out on a MonoVista Confocal Raman microscope spectrometer using a 633 nm helium/neon laser at a 10X working distance. The analyses were carried out on the powder deposited on a glass holder.

Ultraviolet-visible-near infrared spectroscopy: The spectra were obtained in a Cary500 Scan spectrometer (Varian) by using the Cary 500 diffuse reflectance accessory

(integrated sphere). Before the analyses, the samples were compressed to form 0.65 mm thick pellets. The samples were mounted on a black tape and fitted into an integration sphere analysis port. The integration sphere was operated to collect diffuse reflection.

CEES adsorption: The adsorption of CEES was studied in batch experiments. A glass vial containing 150 mg of the sample was introduced into a 160 mL reaction vessel closed with a septum. After hermetically sealing the vessel, CEES (300 μ L) was injected through a septum into a 5 mL beaker in the reaction vessel. The containers were kept under visible light (Xenon lamp, Solar light Co., INC, XPS-150TM) and/or dark at room temperature for 1 or 7 days, depending on the target experiment. The latter was done to ensure the equilibrium of any surface reaction and allow the complete evaporation of the CEES in the container. After equilibrium was reached, vapor phases from the headspace of the containers were sampled with a syringe and injected to GC-MS. Once the vapor sample was taken, the containers were opened and the adsorbent samples were equilibrated in air for 1 h at atmospheric pressure, in the absence of moisture. Finally, the containers with the adsorbents were weighed, and the mass gain as a result of adsorption recorded. The total CEES removal capacity of the materials was calculated after the 7 days experiments as the ratio between the CEES concentration in the containers, and the starting concentration. The percentage of non-bonded volatile compounds was estimated as the difference between the percentages of total removal capacity and the increase in the materials' mass after CEES exposure. Details on the calculations are provided in the Results and Discussion.

Gas Chromatography-Mass spectrometry (GC-MS): The analysis of the relative amounts of CEES and any reaction product present in the vapor phase was carried out using a

GCMS-QP5050A (Shimadzu). The separation of the compounds was performed in XTI-5 column (5% dephenyl-95% dimethyl polysiloxane) of 30 m length, 0.25 mm internal diameter, and 0.25 μm of liquid film thickness. The GC operation program was as follows: an increase from 50 $^{\circ}\text{C}$ to 100 $^{\circ}\text{C}$ at a rate of 5 deg min^{-1} , then the rate was changed to 40 deg min^{-1} up to 280 $^{\circ}\text{C}$. Helium was used as a carrier gas. The injection volume, total flow and, the split ratio were 40 μL , 17.8 mL and 8, respectively. CEES was detected at the elution time of 6.4 min. The mass spectrometer detector was used in an electron impact ionization mode. A calibration curve was prepared by adding 100, 200, 300 and 400 μL of CEES into empty containers. After a complete evaporation of each volume of CEES, the area of the peak at 6.4 min was correlated with the concentration of the CEES.

Conclusions

The results presented in this paper demonstrate the benefits of the incorporation of graphite oxide and aminated graphite oxide to the hydrous ferric oxide for the elimination of CEES from air. The graphene-based phase significantly increased the dispersion of ferric particles, enhancing the adsorption capacity. It is suggested that oxygen and/or nitrogen groups in the graphite oxide act as a nucleation center for the iron aquo-complexes; when the pH increases, the particles grow, around the graphite oxide flakes. The resulting iron/graphite oxide composites have high surface areas and mesopore volumes than the parent hydrous ferric oxide. They are composed mainly of 2 and 6-line ferrihydrite, with minor amounts of hematite and akaganeite. The FT-IR and UV-Vis-NIR results showed the interactions between the hydrous ferric hydroxide and the oxygen groups in the graphite oxide surface. The composites exhibit a high efficiency for

removing CEES vapors from air in both light and dark experimental conditions. Apparently the addition of GO and GOU causes a shift in the band gap energy, causing a clear enhancement in the elimination capacity under visible light radiation. This is associated with the transformation of CEES to simpler/smaller molecules and their migration to smaller pores of higher adsorption energy. Under light exposure, a linear correlation of the amount adsorbed with the micropore volume was found. On the other hand, when the experiments were run in the dark, the total pore volume of composites was found as the most important factor for the adsorption process, owing to the size of the hydrated CEES molecules. The results highlighted the hydrous ferric oxide/graphite oxide composites as interesting materials for the detoxification of CEES vapors. Even though we showed that applicability of these materials for CWA detoxification, their catalytic activity might find potential application for other industrially important processes.

Acknowledgements

This study was supported by the ARO (Army Research Office) grant W911NF-13-1-0225 and NSF collaborative SBET Grant No. 1133112. The assistance of Dr. Jorge Morales during microscopy studies is appreciated.

Notes and references

^a Department of Chemistry, The City College of New York, New York, NY 10031 USA
Tel.:(212)650-6017; Fax: (212)650-6107, E-mail: tbandosz@ccny.cuny.edu

Electronic Supplementary Information (ESI) available: Peak positions on the pK_a distributions, calculations of the crystallite sizes details of the energy band gap calculations, image processing of Figure 3, and CEES chromatograms. See DOI: 10.1039/b000000x/

References

1. T. T. Marrs, R. L. Maynard and F. Sidell, *Chemical Warfare Agents: Toxicology and Treatment*, Wiley, West Sussex, England, 2007.
2. N. A. Monteiro-Riviere, A. O. Inman, M. C. Babin and R. P. Casillas, *J. Appl. Toxicol.*, 1999, **19**, 313-328.
3. A. Roy, A. K. Srivastava, B. Singh, T. H. Mahato, D. Shah and A. K. Halve, *Microporous Mesoporous Mater.*, 2012, **162**, 207-212.
4. M. Fox, Y.-S. Kim, A. A. Abdel-Wahab and M. Dulay, *Catal Lett*, 1990, **5**, 369-376.
5. A. V. Vorontsov, C. Lion, E. N. Savinov and P. G. Smirniotis, *J. Catal.*, 2003, **220**, 414-423.
6. L. Bromberg, N. Pomerantz, H. Schreuder-Gibson and T. A. Hatton, *Ind. Eng. Chem. Res.*, 2014.
7. J. P. Jolivet, M. Henry and J. Livage, *Metal Oxide Chemistry and Synthesis: From Solution to Solid State*, Wiley, West Sussex, England, 2000.
8. J. A. Arcibar-Orozco, J. R. Rangel-Mendez and T. J. Bandosz, *Journal of Hazardous Materials*, 2013, **246–247**, 300-309.
9. B. C. Faust, M. R. Hoffmann and D. W. Bahnemann, *J. Phys. Chem.*, 1989, **93**, 6371-6381.
10. R. M. Cornell and U. Schwetmann, *The Iron Oxides Structure, Properties, Reactions, Occurrences and Uses*, Weinheim, 2003.
11. X. Zhou, H. Yang, C. Wang, X. Mao, Y. Wang, Y. Yang and G. Liu, *J. Phys. Chem. C*, 2010, **114**, 17051-17061.
12. R. R. Gadde and H. A. Laitinen, *Anal. Chem.*, 1974, **46**, 2022-2026.

13. J. A. Arcibar-Orozco, M. Avalos-Borja and J. R. Rangel-Mendez, *Environ. Sci. Technol.*, 2012, **46**, 9577-9583.
14. C. Petit, M. Seredych and T. J. Bandosz, *J. Mater. Chem.*, 2009, **19**, 9176-9185.
15. Y. Zhu, S. Murali, W. Cai, X. Li, J. W. Suk, J. R. Potts and R. S. Ruoff, *Adv. Mater.*, 2010, **22**, 3906-3924.
16. M. Seredych, O. Mabayoje, M. M. Kolesnik, V. Krstic and T. J. Bandosz, *J. Mater. Chem.*, 2012, **22**, 7970-7978.
17. Y. H. Ng, A. Iwase, N. J. Bell, A. Kudo and R. Amal, *Catalysis Today*, 2011, **164**, 353-357.
18. H. Zhang, X. Lv, Y. Li, Y. Wang and J. Li, *ACS Nano*, 2009, **4**, 380-386.
19. A. Lerf, H. He, M. Forster and J. Klinowski, *J. Phys. Chem. B*, 1998, **102**, 4477-4482.
20. M. Seredych, O. Mabayoje and T. J. Bandosz, *Langmuir*, 2011, **28**, 1337-1346.
21. M. Seredych, O. Mabayoje and T. J. Bandosz, *The Journal of Physical Chemistry C*, 2012, **116**, 2527-2535.
22. O. Mabayoje, M. Seredych and T. J. Bandosz, *ACS Appl. Mater. Interfaces*, 2012, **4**, 3316-3324.
23. B. Levasseur, C. Petit and T. J. Bandosz, *ACS Appl. Mater. Interfaces*, 2010, **2**, 3606-3613.
24. T. Jiang, Z. Tao, M. Ji, Q. Zhao, X. Fu and H. Yin, *Catal. Commun.*, 2012, **28**, 47-51.
25. S. Bashkova and T. J. Bandosz, *Ind. Eng. Chem. Res.*, 2009, **48**, 10884-10891.
26. V. K. Singh, M. K. Patra, M. Manoth, G. S. Gowd, S. R. Vadera and N. Kumar, *New Carbon Mater.*, 2009, **24**, 147-152.
27. Y. Zhao, M. Seredych, Q. Zhong and T. J. Bandosz, *ACS Appl. Mater. Interfaces*, 2013, **5**, 4951-4959.
28. J. Fayos, *J. Solid State Chem.*, 1999, **148**, 278-285.
29. Y. Zhao, M. Seredych, Q. Zhong and T. J. Bandosz, *RSC Adv.*, 2013, **3**, 9932-9941.
30. T. Szabó, O. Berkesi and I. Dékány, *Carbon*, 2005, **43**, 3186-3189.
31. U. Bohner and G. Zundel, *J. Phys. Chem.*, 1985, **89**, 1408-1413.
32. B. H. Stuart, *Infrared Spectroscopy: Fundamentals and Applications*, Wiley, West Sussex, England, 2004.
33. B. Konkena and S. Vasudevan, *J. Phys. Chem. Lett.*, 2012, **3**, 867-872.

34. D. Masih, Y. Seida and Y. Izumi, *Water Air Soil Pollut: Focus*, 2009, **9**, 203-211.
35. R. Kaiser, A. Kulczyk, D. Rich, R. J. Willey, J. Minicucci and B. MacIver, *Ind. Eng. Chem. Res.*, 2007, **46**, 6126-6132.
36. I. Carabante, M. Grahn, A. Holmgren, J. Kumpiene and J. Hedlund, *Colloids Surf., A*, 2009, **346**, 106-113.
37. R. M. Cornell and U. Schwertmann, *The Iron Oxides: Structure, Properties, Reactions, Occurrences and Uses*, Wiley, Weinheim, Germany, 2006.
38. R. L. Penn, *Science*, 2007, **316**, 1704-1705.
39. D. E. Janney, J. M. Cowley and P. R. Buseck, *Clays Clay Miner.*, 2000, **48**, 111-119.
40. L. Charlet and A. A. Manceau, *J. Colloid Interface Sci.*, 1992, **148**, 443-458.
41. T. J. Bandosz, *Pol. J. Chem.*, 1998, **72**, 1202-1214.
42. K. Rout, M. Mohapatra and S. Anand, *Dalton Transactions*, 2012, **41**, 3302-3312.
43. J. D. Russell, *Clay Miner.*, 1979, **14**, 109-114.
44. B. C. Smith, *Infrared Spectral Interpretation: A Systematic Approach*, Taylor & Francis, Boca Raton, 1998.
45. L. Mazzetti and P. J. Thistlethwaite, *J. Raman Spectrosc.*, 2002, **33**, 104-111.
46. K. N. Kudin, B. Ozbas, H. C. Schniepp, R. K. Prud'homme, I. A. Aksay and R. Car, *Nano Letters*, 2007, **8**, 36-41.
47. A. Kaniyoor, T. T. Baby and S. Ramaprabhu, *J. Mater. Chem.*, 2010, **20**, 8467-8469.
48. F. Banhart, J. Kotakoski and A. V. Krasheninnikov, *ACS Nano*, 2010, **5**, 26-41.
49. A. Cortijo and M. A. H. Vozmediano, *Nucl. Phys. B*, 2007, **763**, 293-308.
50. J. Torrent and V. Barrón, *Diffuse reflectance spectroscopy of iron oxides*, Boca Raton, 2002.
51. A. E. Morales, E. S. Mora and U. Pal, *Rev. Mex. Fis. S* 2007, **53**, 18-22.
52. Y. Zhang, N. Zhang, Z.-R. Tang and Y.-J. Xu, *ACS Nano*, 2012, **6**, 9777-9789.
53. O. Mabayoje, M. Seredych and T. J. Bandosz, *Applied Catalysis B: Environmental*, 2013, **132-133**, 321-331.
54. S. Y. Treschev, P.-W. Chou, Y.-H. Tseng, J.-B. Wang, E. V. Perevedentseva and C.-L. Cheng, *Applied Catalysis B: Environmental*, 2008, **79**, 8-16.
55. Y. Nakano, S. Saeki and T. Morikawa, *Appl. Phys. Lett.*, 2009, **94**, -.
56. P. Rani and V. K. Jindal, *RSC Adv.*, 2013, **3**, 802-812.

57. T. P. Chow and R. Tyagi, *Electron Devices, IEEE Transactions on*, 1994, **41**, 1481-1483.
58. J.-P. Jolivet, C. Chaneac and E. Tronc, *Chemical Communications*, 2004, 481-483.
59. W. S. Hummers and R. E. Offeman, *J. Am. Chem. Soc.*, 1958, **80**, 1339-1339.
60. M. M. Dubinin, in *Progress in Surface and Membrane Science*, eds. J. F. D. D.A. Cadenhead and R. M.D, Elsevier, New York, US, 1975, pp. 1-70.
61. E. P. Barrett, L. G. Joyner and P. P. Halenda, *J. Am. Chem. Soc.*, 1951, **73**, 373-380.
62. C. Contescu, J. Jagiello and J. A. Schwarz, *Langmuir*, 1993, **9**, 1754-1765.
63. T. J. Bandosz, J. Jagiello, C. Contescu and J. A. Schwarz, *Carbon*, 1993, **31**, 1193-1202.
64. J. Jagiello, *Langmuir*, 1994, **10**, 2778-2785.

Captions to the Tables

Table 1. The parameters of porous structure calculated from nitrogen adsorption isotherms.

Table 2. An increase in the weight of the composites/amounts adsorbed after CEES exposure under visible light and in the dark together with the adsorption capacities and the percentages of CEES removed and transformed into volatile compounds on the surface of the samples studied after 7 days of experiments under visible light exposure.

Captions to the Figures

Figure 1. A) X-Ray diffraction patterns, B) FTIR spectra, C) Proton binding curves and D) pK_a distributions for the graphite oxide (GO) and aminated graphite oxide (GOU).

Figure 2. A) Pore size distributions for the ferric hydrous oxide and the composites with graphite oxide. B) X-Ray diffraction patterns of the hydrous ferric oxide and the composites with graphite oxide, ● 6-line ferrihydrite, ☆ -Akaganeite.

Figure 3. SEM images of the surfaces of the samples studied. The enlarged area in the image of FeO-GOU corresponds to a band-pass filter image obtained applying Fast Fourier Transform (FFT) of the area marked in the square. A mask removing at high and low frequencies was applied, and the inverse FFT yielded the band-passed image (See Supplementary Information for detail of the image processing).

Figure 4. A) TEM image of FeO-G, B) a highlighted zone showing the graphen phase in the FeO-GO and a small crystal of the iron hydroxide phase. C) TEM image of FeO-GOU. D) Electron diffraction pattern revealing some degree of crystallinity in the samples. E) Image of the FeO-GOU nanocrystals. F) Image of the nanocrystals, the inset represents the inverse Fourier transform of the selected area, the fridge distance is of 0.25 nm.

Figure 5. Potentiometric titration results: proton binding curves (A) and pK_a distributions (B).

Figure 6. FTIR-ATR spectra for the materials studied.

Figure 7. Raman spectra of FeO and its composites with GO or GOU.

Figure 8. A) UV-Vis-NIR spectra of the synthesized composites, B) $[F(R_{\infty})hv]^2$ versus photon energy. The lines show the cut-off employed to calculate the band gap energy.

Figure 9. Interactions of HFO with GO surface, A) Nucleation of iron hexaaquo complexes, B) oxygen bridge between oxygen groups in the GO and iron complexes, C) Condensation of the hydrous ferric oxide particles, and D) Evolution of porosity in the HFO aggregates.

Figure 10. Dependence of the amount adsorbed (after 24 h of equilibrium) on the volume of pores in the materials after CEES exposure. A) under the light exposure; B) experiments in dark.

High surface area composites consisting of iron oxyhydroxides and graphite oxide/ aminated graphite oxide are efficient media for adsorption/decontamination of a mustard gas surrogate (CEES).

Keyword

Iron hydroxide/graphite oxide composites.

*Javier A. Arcibar-Orozco and Teresa J. Bandosz**

Visible Light Enhanced Removal of Sulfur Mustard Gas Surrogate from a vapor phase on Novel Hydrated Ferric Oxide/Graphite Oxide Composites